

Location-aware Adaptive Denormalization: A Deep Learning Approach For Wildfire Danger Forecasting

Mohamad Hakam Shams Eddin, Ribana Roscher, *Member, IEEE* and Juergen Gall, *Member, IEEE*

Abstract—Climate change is expected to intensify and increase extreme events in the weather cycle. Since this has a significant impact on various sectors of our life, recent works are concerned with identifying and predicting such extreme events from Earth observations. This paper proposes a 2D/3D two-branch convolutional neural network (CNN) for wildfire danger forecasting. To use a unified framework, previous approaches duplicate static variables along the time dimension and neglect the intrinsic differences between static and dynamic variables. Furthermore, most existing multi-branch architectures lose the interconnections between the branches during the feature learning stage. To address these issues, we propose a two-branch architecture with a Location-aware Adaptive Denormalization layer (LOADE). Using LOADE as a building block, we can modulate the dynamic features conditional on their geographical location. Thus, our approach considers feature properties as a unified yet compound 2D/3D model. Besides, we propose using an absolute temporal encoding for time-related forecasting problems. Our experimental results show a better performance of our approach than other baselines on the challenging FireCube dataset.

Index Terms—Machine learning, remote sensing, climate science, wildfire, convolutional neural network, adaptive denormalization, time encoding.

I. INTRODUCTION

THERE is a general expectation that weather and climate extremes will change their patterns and frequencies in the future [1]–[4]. This is particularly the case for the Mediterranean region, which has been identified as a hot spot for climatic changes [5]–[7]. Because extreme weather events can impose short- and long-term risks in our Earth system, predicting these risks such as droughts, windstorms, and wildfires has become recently more relevant. In particular, wildfire forecasting constitutes one of the open challenges for risk assessment and emergency response [8]–[10]. Wildfire forecasting refers to the task of fire-susceptibility mapping using key remote sensing, meteorological, and anthropogenic variables [11]. Building an integrated modeling system of the Earth should also consider wildfire events to comprehend the origin of past patterns better and predict future ones [12]. Unlike typical prediction tasks, understanding when weather conditions have a high tendency to cause fire events addresses more complexities; among these are the stochastic nature of fire events [13] and fire drivers, which are time-dependent and

inter-correlated across variables [14]. Moreover, the prediction model should consider difficulties like a high false positive error rate, uncertainty, and class imbalance.

In recent years, many works leveraged classical machine learning approaches to solve the task [11]. More recently, deep learning methods [15] have become popular since they can handle large multivariate datasets more efficiently and are able to learn highly complex relationships between observations and the predicted outcome. In the context of wildfire danger forecasting, Prapas et al. [16] and Kondylatos et al. [13] proposed to use recurrent neural networks in combination with 2D convolutions to exploit both temporal and spatial context. These approaches, however, do not distinguish between the different input variables. Static variables like elevation, which barely change over time, are simply copied and concatenated with dynamic variables like surface temperature. This results not only in a highly redundant input to the network, but it also neglects strong causal effects between static and dynamic variables. For instance, the surface temperature strongly depends on the geographical location, which is described by static variables.

In this work, we thus propose a convolutional neural network for wildfire danger forecasting that handles static and dynamic variables differently. Since the static variables do not change over time, they are processed by a branch consisting of 2D convolutions while the dynamic variables are processed by the second branch with 3D convolutions as illustrated in Fig. 1. To address the causal effect of static variables on dynamic variables, we introduce *feature modulation* for the dynamic variables where the modulation parameters are generated dynamically and conditionally on the geographical location. We thus name this method Location-aware Adaptive Denormalization (LOADE). In addition, we encode the date of the forecasting during a year by an absolute time encoding. Both LOADE and the time encoding can be implemented as plugin layers in different deep learning architectures. We view our model as a generic architecture that can be used for other time-dependent forecasting tasks with static and dynamic variables. We conduct extensive experiments on the FireCube dataset [17] where our approach outperforms previous works. We achieve an overall improvement of up to **5.72%** in precision, **3.9%** in F1-score, **0.63%** in AUROC, and **1.15%** in OA on the test set. The source code will be released upon acceptance.

The rest of this paper is organized as follows. Section II reviews the related literature. Section III provides information about the used dataset. The proposed method is described in detail in Section IV. The experimental results and ablation

Manuscript created December, 2022; This work was funded by the Deutsche Forschungsgemeinschaft (DFG, German Research Foundation) – SFB 1502/1–2022 - Projekt-nummer: 450058266.

Corresponding author: Mohamad Hakam Shams Eddin. The authors are with the University of Bonn, Germany (e-mail: {shams, gall}@iai.uni-bonn.de) and the Research Center Jülich (e-mail: ribana.roscher@uni-bonn.de).

Preprint. Under review.

study are provided in Section V and Section VI, respectively. Finally, conclusions and outlook are given in Section VII.

II. RELATED WORKS

A. Wildfire Danger Forecasting

Wildfire forecasting or wildfire-susceptibility mapping from remote sensing and Earth observations data is a very important topic for wildfire management [11]. We briefly review some prior related works in this direction. Iban et al. [18] relied on traditional machine learning to generate susceptibility maps. Jiang et al. [19] proposed a deep learning approach based on a Multi-Layer Perceptron (MLP) and included a comparison with traditional machine learning algorithms. In Le et al. [20], a similar MLP-based approach was presented to generate a forest fire danger map. Zhang et al. [21] used a convolutional neural network (CNN) and extended their work later to predict fire susceptibility at the global level [22]. Other works with CNN were conducted in Bjånes et al. [23] and Bergado et al. [24]. Furthermore, Huot et al. [25] approached the problem as a scene classification task using U-Net models to predict wildfire spreading. Their approach operates directly on the whole scene. A similar approach based on a U-Net++ model for global wildfire forecasting was proposed in Prapas et al. [26]. More recently, Prapas et al. [16] and Kondylatos et al. [13] proposed to use LSTM-based (Long-Short Term Memory) approaches. They exploited both temporal and spatio-temporal context by applying recurrent LSTM and ConvLSTM models. They did not consider the whole scene at once but rather classification of one pixel at a time (pixel-level).

Unlike these works, we do not treat all observation variables in the same way, but we propose a deep learning model that handles different types of variables in separated 2D and 3D CNN branches. We assume that the dataset contains static and dynamic variables, which we argue is the case for most datasets. Similar to Prapas et al. [16] and Kondylatos et al. [13], we also formulate the problem as pixel-level classification taking into account the spatio-temporal local context around the target pixel.

B. Multi-Branch Neural Networks

When deep learning is applied to potentially multi-source remote sensing-based Earth observation data, multi-branch neural networks are a commonly used framework. This is mainly because such networks enrich representation learning and provide discriminative learning perspectives of the input variables [27]. In addition, an important aspect of the multi-branch design is the capability to adapt some parts of the model to a specific type of input. The general framework generates features from each branch and fuses these features in the network to obtain a unified feature vector. This fused representation is used as input to the subsequent layers. In Gaetano et al. [28], a two-branch 2D CNN network is proposed to handle panchromatic information along with multi-spectral ones for image classification. Tan et al. [29] reduced the depth of a semantic segmentation classifier by applying consecutive blocks, each containing three CNN branches. A similar objective can be found in Zhao et al. [27], where

the network complexity was reduced via weight sharing and self-distillation (SD) embedding. In this way, only the main branch is used during inference, which inherits the knowledge of trained subbranches and has a close performance to an ensemble model. For hyperspectral image classification, Xu et al. [30] introduced a model called Spectral-Spatial Unified Network (SSUN). In their model, spectral features are learned by a grouping-based LSTM, and spatial features are learned by a 2D CNN. Shen et al. [31] used separated spectral and spatial convolutional branches for hyperspectral input (S^2 CDELM). They based their framework on the extreme learning machine (ELM). Unlike common backpropagation algorithms, they used a single hidden layer feed-forward model. A multi-branch architecture was also explored for image fusion. Liu et al. [32] proposed a two-stream CNN called (StfNet). They investigated the task of spatio-temporal image fusion. Their network takes a coarse image input along with its neighboring images to predict the reconstructed fine image. Some works adapted a multi-branch architecture to construct a multi-scale feature vector. In Gan et al. [33], a dual-branch CNN with different filter kernel sizes was used as an autoencoder. Thus, the input image could be processed at different scales. Tang et al. [34] proposed a multi-scale Gaussian pyramid to handle hyperspectral input. They used the Gaussian pyramid to obtain multi-scale images which are then processed by ResNet modules [35]. In this way, spatial features can be learned at different scales. They further used a second branch, which performs a discrete wavelet transform on the spectral input followed by an LSTM module [36]. The spatial and spectral features are then fused and processed by an MLP to obtain the final classification result. For short-term multi-temporal image classification, Zheng et al. [37] addressed the task through a Multi-temporal Deep Fusion Network (MDFN). In their framework, the LSTM-based branch is used to learn temporal-spectral features. At the same time, temporal-spatial and spectral-spatial information is learned via a joint 3D-2D CNN with two branches. Furthermore, some works employed attention mechanisms with multi-branch architectures [38]–[40]. When attention is applied, it drives the model to focus more on regions of interest. The former described methods [28]–[34], [37], [38] except of Zhao et al. [27], Zhu et al. [39], and Deng et al. [40] did not consider linking information between branches during the feature learning stage. This limits the gradient flow and disentangles the correlations between the learned features.

This paper proposes an architecture composed of two CNN branches for a forecasting task. A 2D branch is used to learn spatial features from static variables. At the same time, a 3D branch is used to learn spatio-temporal features from dynamic variables, which vary along the input temporal dimension. The branches are further linked via adaptive modulation layers to model causal effects of static variables on dynamic variables.

C. Conditional Normalization

Since the introduction of normalization techniques in deep learning, they became a basic building block in many state-of-the-art models. Common normalization methods include

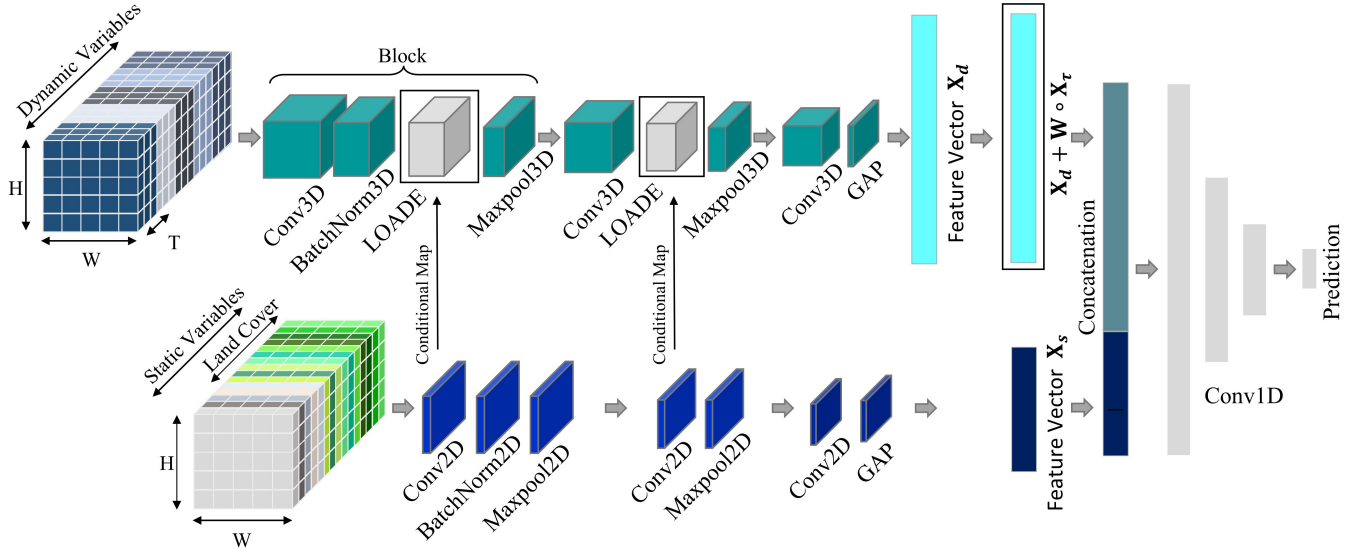


Fig. 1. Overview of the proposed approach. Our network handles static and dynamic variables by two branches. For the static branch, we use 2D convolutions whereas we use 3D convolutions for the dynamic branch since the dynamic variables change over time. Since dynamic variables like surface temperature strongly depend on static variables like elevation, we modulate the dynamic features conditioned on the static features at two blocks (LOADE). This makes the model location-aware since the static variables contain geographic data like land cover. The feature vector \mathbf{X}_d from the dynamic branch is combined with a weighted temporal encoding vector \mathbf{X}_τ before it is concatenated with the static feature vector \mathbf{X}_s . The concatenated vector serves as input to fully connected layers that predict the probability of a wildfire.

batch normalization [41], group normalization [42], instance normalization [43], and layer normalization [44]. It has been shown empirically that normalization layers help with model optimization and regularization. Through normalization layers, the activation maps inside the model are normalized to follow a normal distribution with zero mean. After that, the normalized activation maps are modulated or denormalized by learnable affine transformation parameters. These parameters vary across channels and are learned based on the running training statistics together with the model parameters. Therefore, such a normalization method is called unconditional. Compared to popular unconditional normalizations, there exist conditional normalization techniques which aim to learn affine parameters conditionally on external input. In the field of computer vision, conditional normalization is often used for image synthesis and style transformation [45]–[58]. More recently, Marín and Escalera [59] adapted the conditional normalization from Wang et al. [46] and Park et al. [45] to generate high-resolution satellite images. We use the conditional normalization in a very different way than [45], [46], [59]. While these works focus on synthesizing an image using the segmentation map as conditional input, we aim to modulate dynamic features conditioned on static features.

D. Temporal Positional Encoding

A plethora of studies exist about temporal modelling in remote sensing [60]–[63]. Recently, the self-attention model, also known as Transformer and first presented by Vaswani et al. [64] for natural language processing, has become a natural choice to handle sequential data, which includes a positional encoding. In the field of remote sensing, many works showed the benefits of adapting positional encoding for time-dependent image classification (Garnot et al. [65],

Garnot and Landrieu [66]), panoptic segmentation (Garnot and Landrieu [67]), and image generation (Dress et al. [68]). In their work, each image was given an encoded time vector according to its position with respect to a reference point, i.e., the first acquisition time step. Nyborg et al. [69] used the calendar time (day of the year) to provide positional information within the sequence. They also proposed to learn or estimate time shifts between geographically distant regions to enhance the generalization further. In another work, Nyborg et al. [70] used the thermal time, which is obtained by accumulating daily average temperatures over the growing season, for crop classification. These approaches require the positional encoding since the temporal information is otherwise lost within a transformer model. While 3D CNNs consider the temporal order of the input such that a positional encoding is not necessary, we show in this work that temporal encoding is also useful for time-dependent forecasting.

III. DATASET

There are only very few publically available datasets for wildfire forecasting and they differ significantly in the observational variables, the spatial and temporal resolution, and the task that needs to be addressed. A related dataset is the Next Day Wildfire Spread dataset [25] where the task is to predict wildfire spread. It is formulated as a scene classification task and not as a pixel-wise wildfire forecasting task as it is proposed in the FireCube dataset [17] and addressed in this work. The FireCube dataset was first published in Prapas et al. [16] and extended later in Kondylatos et al. [13]. It includes multivariate spatio-temporal data streams with 90 variables from the years 2009–2021 with a resolution of $1 \text{ km} \times 1 \text{ km} \times 1 \text{ day}$. The area is $1253 \text{ km} \times 983 \text{ km}$, covering parts of the Eastern Mediterranean. The observational variables

include meteorological data [71], satellite-derived products [72], [73], topographic features [74], human-related activities [75], and historical fire records [76], [77]. In addition, Copernicus Corine Land Cover (CLC) [78] and Fire Weather Index (FWI) [79] are provided. The target is to predict for each pixel if a wildfire will ignite and become large ($> 0.3 \text{ km}^2$) in the next day. The task is equivalent to binary classification, where the positive class represents a wildfire event.

Since wildfire forecasting is essentially an imbalanced classification task, the authors of [13] extracted samples as follows: For a target day $T+1$, the static variables form a patch of $25 \text{ km} \times 25 \text{ km}$ centered around the target pixel at day T . In contrast, the dynamic variables consist of $25 \text{ km} \times 25 \text{ km} \times 10$ days time series of observations from days $T-9$ until T . For each positive sample, a few negative samples from different locations are sampled. Although the negatives are from different locations, they are sampled from regions that have a similar land cover distribution as the positive sample to make the task more difficult.

Overall the dataset includes 71471 samples for training (13518 positives and 57953 negatives for the years 2009-2018), 6430 samples for validation (1300 positives and 5130 negatives for the year 2019) and 42820 samples for testing (1228 positives and 4860 negatives for the year 2020 and 4407 positives and 32325 negatives for the year 2021). The year 2021 in the test set contains an extreme wildfire season in Greece [13], [80]. The extracted samples are available in [81].

In this paper, we use from the described dataset the same variables as in Kondylatos et al. [13]. This includes the following:

- 15 static variables:
 - Digital elevation model (DEM) and Slope [74].
 - Distance to roads, distance to waterway, and population density [75].
 - Copernicus Corine Land Cover variables representing the fractions of classes for each pixel. This gives 10 variables per pixel [78].
- 10 dynamic variables:
 - Day and night land surface temperature [73].
 - Normalized difference vegetation index (NDVI) [72].
 - Soil moisture index [82].
 - Maximum 2m temperature, maximum wind speed, minimum relative humidity, total precipitation, maximum 2m dew-point temperature, and maximum surface pressure [71].

IV. METHODOLOGY

Problem formulation. Given a multivariate spatiotemporal data cube $\mathcal{C}(\{V, T, W, H\})$, where H and W are the spatial extensions of the cube, T is the temporal extension in the past for the time series $1, 2, \dots, T$, and V is the number of variables (static and dynamic), our aim is to learn a mapping function f approximated by a neural network that can predict the probability of a wildfire event to start $Y_{T+1} \in [0, 1]$ at the center of $W \times H$ for the target day $T+1$:

$$f : \mathcal{C}(\{V, T, W, H\}) \rightarrow Y_{T+1} \quad (1)$$

To achieve this, we propose a spatiotemporal 2D/3D CNN with two branches as illustrated in Fig. 1. First, the network design is introduced in Section IV-A. Then, the Location-aware Adaptive Denormalization layer (LOADE), which is the core of our work is explained in detail in Section IV-B. Finally, Section IV-C describes how to integrate the absolute temporal encoding (TE) into the model.

A. 2D/3D Two-Branch CNN

As shown in Fig. 1, our network consists of two branches that process dynamic and static variables, respectively. We denote the data cube with dynamic variables by $\mathcal{C}(\{V_d, T, W, H\})$ and the data cube with static variables by $\mathcal{C}(\{V_s, W, H\})$. As in previous works, we normalize the input channel-wise to the range $[0, 1]$. Since the static variables do not have a time component, we use 2D convolutions for the static branch and 3D convolutions for the dynamic branch. More in detail:

Dynamic branch. The dynamic branch takes the variables V_d which vary over time as input. It consists of 3 blocks; each block has a 3D convolution with a 3×3 kernel size followed by a ReLU activation function and a 3D max pooling layer. To reduce overfitting, we use global average pooling (GAP) [83] at the end of the last block. We denote the feature vector learned from this branch as $\mathbf{X}_d \in \mathbb{R}^{256}$.

Static branch. In parallel to the dynamic branch, the static branch has a similar architecture. However, 2D convolutions are used instead of 3D ones. We denote the feature vector learned from this branch as $\mathbf{X}_s \in \mathbb{R}^{128}$. Note that the dimensionality of the static feature vector is lower than the dimensionality of the dynamic feature vector since the input data cube is smaller.

In a nutshell, the dynamic- and static branch are two functions f_d and f_s , respectively:

$$f_d : \mathcal{C}(\{V_d, T, W, H\}) \rightarrow \mathbf{X}_d \quad (2)$$

$$f_s : \mathcal{C}(\{V_s, W, H\}) \rightarrow \mathbf{X}_s \quad (3)$$

For the dynamic feature vector we add an absolute temporal encoding \mathbf{X}_τ , which will be described in Section IV-C. The two feature vectors are then concatenated and fed into 4 classification layers with 1D convolutions of kernel size 1. The layers reduce the dimensionality from 384 to 256, 128, 32, and 2. To reduce overfitting, we use dropout with a dropout probability $p = 0.5$ for the 1D convolutional layers except the last two layers. Finally, a softmax activation is used after the last classification layer to predict the probability of a wildfire. For training, we use the unweighted negative log likelihood loss. In addition, we use a batch normalization layer [41] for the 1st block of each branch. More implementation details are given in Section V.

In the following, we discuss the Location-Aware Adaptive Denormalization (LOADE) that modulates the dynamic features based on the static features and the already mentioned absolute temporal encoding.

B. Location-Aware Adaptive Denormalization (LOADE)

In general, dynamic variables are correlated with the geographic location, i.e., temperature and pressure change with

elevation, soil moisture and NDVI vary with land cover, and humidity is correlated with some static variables like the waterway distance. Since the dynamic variables depend on the static variables and not vice versa, we aim to exploit this knowledge in our approach. This is done by learning to denormalize the dynamic features based on the location-dependent static features. To this end, we propose a conditional denormalization technique for remote sensing data called Location-aware Adaptive Denormalization (LOADE).

We first describe a batch-normalization [41] where the activation map is normalized before it is modulated by scale γ and bias β . Let $z_d^i \in \mathbb{R}^{N \times K^i \times D^i \times W^i \times H^i}$ be an activation map in the i -th block of the dynamic branch and $z_s^i \in \mathbb{R}^{N \times K^i \times W^i \times H^i}$ be an activation map of the corresponding i -th block in the static branch, where N denotes the batch size, K^i the number of channels, and D^i , W^i and H^i denote the depth, width, and height of the activation map z^i , respectively. In case of the dynamic branch, the normalization is given by the following equation ($n \in \{1, \dots, N\}$, $k \in \{1, \dots, K^i\}$, $t \in \{1, \dots, D^i\}$, $w \in \{1, \dots, W^i\}$, $h \in \{1, \dots, H^i\}$):

$$\left(\frac{z_{d(n,k,t,w,h)}^i - \mu_k}{\sigma_k} \right) \cdot \gamma_k + \beta_k \quad (4)$$

where $z_{d(n,k,t,w,h)}^i$ is the activation before the normalization, μ_k and σ_k are the computed mean and standard deviation of channel k , i.e., computed over the tensor $D^i \times W^i \times H^i$ and all samples n in the batch, and γ_k and σ_k are the learnable modulation parameters.

In our case, we aim to learn a modulation of the dynamic features $z_{d(n,k,t,w,h)}^i$ at i -th block where the modulation parameters $\gamma_{s(n,k,w,h)}^i$ and $\beta_{s(n,k,w,h)}^i$ depend on the corresponding static features $z_{s(n,k,w,h)}^i$:

$$z_{d(n,k,t,w,h)}^i \cdot \gamma_{s(n,k,w,h)}^i + \beta_{s(n,k,w,h)}^i. \quad (5)$$

In contrast to (4), the modulation parameters $\gamma_{s(n,k,w,h)}^i$ and $\beta_{s(n,k,w,h)}^i$ vary with respect to sample n in the batch, the location (w, h) , and across channel k , but they are constant over time t . Furthermore, they are conditioned on the static features z_s^i . We thus call z_s^i the conditional map for the modulation.

The way how $\gamma_{s(n,k,w,h)}^i$ and $\beta_{s(n,k,w,h)}^i$ are computed is illustrated in Fig. 2. First, the conditional map z_s^i is normalized channel-wise as following:

$$\hat{z}_{s(n,k,w,h)}^i = \frac{z_{s(n,k,w,h)}^i - \mu_k^i}{\sigma_k^i} \quad (6)$$

where

$$\mu_k^i = \frac{1}{NW^iH^i} \sum_{n=1}^N \sum_{w=1}^{W^i} \sum_{h=1}^{H^i} z_{s(n,k,w,h)}^i \quad (7)$$

$$\sigma_k^i = \sqrt{\frac{1}{NW^iH^i} \sum_{n=1}^N \sum_{w=1}^{W^i} \sum_{h=1}^{H^i} (z_{s(n,k,w,h)}^i - \mu_k^i)^2}. \quad (8)$$

Afterward, $\hat{z}_{s(n,k,w,h)}^i$ is projected by two convolutional layers with K^i filters to compute $\gamma_{s(n,k,w,h)}^i$ and $\beta_{s(n,k,w,h)}^i$.

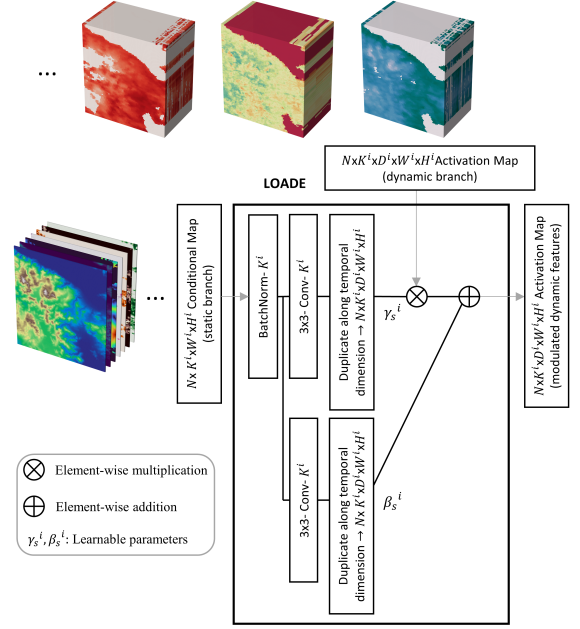


Fig. 2. Illustration of the Location-aware Adaptive Denormalization layer (LOADE) when using the conditional map from the static branch. The conditional map of the static branch and the activation map of the dynamic branch have the same N , K^i , W^i , and H^i dimensions. BatchNorm denotes a batch normalization layer. 3×3 -Conv- K^i denotes a convolution layer with a kernel size of 3×3 and K^i output channels.

In our implementation, these modulation parameters are then duplicated along the temporal dimension to match the depth D^i of z_d^i such that (5) can be computed.

We add the Location-aware Adaptive Denormalization layer (LOADE) in the first two blocks as shown in Fig. 1. The activation maps of the dynamic branch are normalized only in the 1st block and modulated in both the 1st and 2nd blocks. The impact of the blocks where the LOADE layer is added is evaluated in Table VI.

In the experimental section, we also evaluate a variant of LOADE that is not conditioned on the intermediate features of the static branch as shown in Figs. 1 and 2, but on the static variables directly as shown in Fig. 3. In this case, the conditional map has different spatial dimensions and number of channels compared to the features in the dynamic branch, i.e., the conditional maps consist of C variables and have $W^s \times H^s$ spatial dimensions. In this respect, the conditional map ($W^s \times H^s$) is first resized to match the spatial dimensions ($W^i \times H^i$) of the activation map from the dynamic branch. We use the nearest-neighbor method for the down-sampling. The resized conditional map is then fed into a convolutional layer with 3×3 kernel size to double the number of channels, i.e., $2 \times C$. Finally, as in the previous version of LOADE, the conditional map is normalized, projected by two convolutional layers, and duplicated along the temporal dimension to compute $\gamma_{s(n,k,w,h)}^i$ and $\beta_{s(n,k,w,h)}^i$. The impact of different conditional maps using the variants of LOADE is evaluated in Table IV.

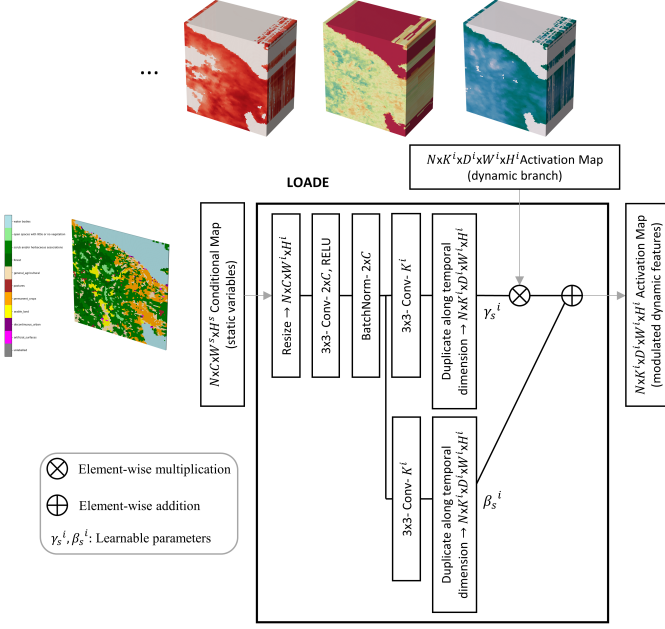


Fig. 3. Illustration of the Location-aware Adaptive Denormalization layer (LOADE) when using C static variables directly for modulation. In this case, there is a mismatch between the dimensions of the conditional map and the activation maps of the dynamic branch at the i -th block. To adjust for the spatial resolution, we resize the conditional map using nearest-neighbor down-sampling to match the resolution of the activation map from the dynamic branch. The convolution layer takes C channels as input and generates an output with K^i channels.

C. Absolute Temporal Encoding (TE)

Some extreme events in the climate model have a dependent relation on time [14], [84]. This is also the case for the FireCube dataset [17] where wildfire events vary from month to month and occur more frequently in the summer time as shown in Fig. 5. So far, the network does not consider an absolute time like the day of the year. Instead, for any forecast day $T+1$, the last 10 days are used as observation but the network does not have the information what day during the year T is.

As shown in Fig. 1, we add this information to the dynamic branch before we concatenate the static and dynamic features. To encode the day of the year, we use the standard fixed sinusoidal-based encoding by Vaswani et al. [64], i.e., we pre-compute for each day of the year $\tau \in [0, 365]^1$, which is extracted from T , the absolute temporal encoding vector $\mathbf{X}_\tau \in \mathbb{R}^{256}$:

$$\mathbf{X}_\tau(2j) = \sin(\tau/10^{2j/256}), \quad (9)$$

$$\mathbf{X}_\tau(2j+1) = \cos(\tau/10^{2j/256}), \quad (10)$$

where j is the embedding dimension. Each even dimension results from a sine function, while each odd dimension results from a cosine function. This allows τ to have a smooth and yet unique encoding for every time step, i.e., each day of a year. Note that the vector has the same size as \mathbf{X}_d .

¹We consider February 29 for the encoding.

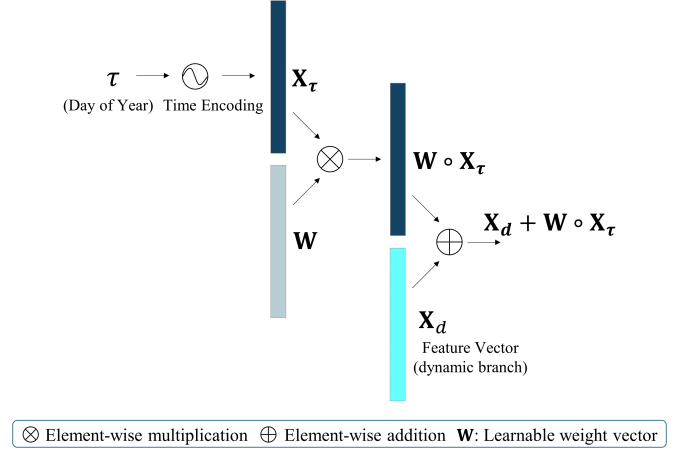


Fig. 4. Illustration of how the absolute temporal encoding is added in the model. The day of year τ is encoded into a vector \mathbf{X}_τ and each element is weighted by the learned weight vector \mathbf{W} . The weighted vector is then added to the dynamic feature vector \mathbf{X}_d .

In order to add the absolute time encoding vector \mathbf{X}_τ to the dynamic feature vector \mathbf{X}_d , we weight each element of the vector by a learnable weight vector $\mathbf{W} \in \mathbb{R}^{256}$:

$$\mathbf{X}_d + \mathbf{W} \circ \mathbf{X}_\tau, \quad (11)$$

where \circ denotes the Hadamard product, i.e., element-wise multiplication. Fig. 4 illustrates how the temporal embedding is added to the model.

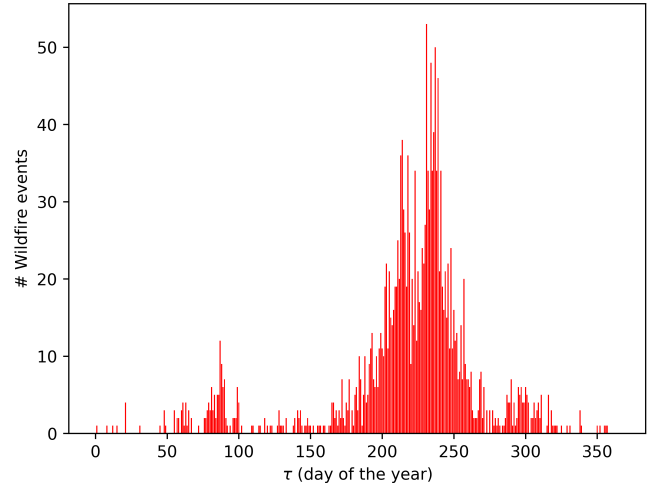


Fig. 5. Distribution of the wildfire events per day between 06/03/2009 and 29/08/2021 (FireCube dataset).

V. EXPERIMENTAL RESULTS AND ANALYSIS

Implementation Details. The network is trained with an unweighted negative log likelihood loss using the Pytorch framework [85] with a learning rate $lr = 0.00003$ and Adam optimizer ($\beta_1 = 0.9$, $\beta_2 = 0.999$) [86] with a weight decay $\lambda = 0.02$. We use a batch size of $N = 256$. All models were trained on a single NVIDIA GeForce RTX 3090 GPU.

Performance Metrics. As described in Section III, we use the FireCube dataset [17]. We follow the same protocol for

quantitative comparison as in Prapas et al. [16] and Kondylatos et al. [13]. The evaluation metrics are precision, recall, and F1-score, calculated for the positive class that represents a wildfire event. In addition, we report true positives (TP), false positives (FP), true negatives (TN), and false negatives (FN). Moreover, we provide the overall accuracy (OA), and the area under the receiver operating characteristic curve (AUROC) as evaluation metrics. OA is the accuracy obtained on all negative and positive samples in the test set. The AUROC describes the true positive rate (TPR) against the false positive rate (FPR) within multiple thresholds in a one value.

A. Comparison with Baselines

We compare our approach to the algorithms reported on the described dataset in Kondylatos et al. [13]. This includes two deep learning models, namely LSTM [36] and ConvLSTM [60], and two classical machine learning classifiers, namely random forests (RF) [87] and XGBoost [88]. For further details regarding the architectures and hyper-parameters of the models, we refer to the work of Kondylatos et al. [13]. In order to demonstrate the benefit of treating static and dynamic variables differently, we also compare with a one-branch 3D CNN model, where we duplicate the static variables along the temporal dimension and concatenate them together with the dynamic variables to form a single data cube. To ensure a fair comparison, all baselines were re-implemented and trained on the same samples with a fixed random seed. We do not use any augmentation technique. The quantitative results of our experiments are provided in Table I. The results of the proposed 2D/3D CNN are shown with and without absolute temporal encoding (TE).

We can observe that the proposed 2D/3D CNN outperforms the other methods for most metrics on the validation and testing sets. Only for 2020, AUROC is slightly higher for ConvLSTM and LSTM achieves a higher recall, but at the cost of a very low precision. In comparison with other deep learning methods, LSTM has even the highest number of false positives for all years. The main weakness of LSTM lies in the fact that it does not consider the spatial context. RF and XGBoost have the same disadvantage as LSTM, but even a weaker temporal model and thus perform worse than LSTM. Most interesting is the comparison to 3D CNN since it uses the same 3D CNN structure but only one branch, i.e., it treats static variables like dynamic variables. The results show that the proposed approach with two branches outperforms the single branch architecture for all metrics and all years. This demonstrates the importance of treating static variables differently than dynamic variables. Adding the absolute temporal encoding (TE) to the model substantially reduces FP at the cost of decreasing TP. This is also reflected in the precision and recall.

In Table II, we present additional experimental results alongside the memory footprint as the number of parameters (# Params) and the expected inference time, which is estimated as samples per millisecond (# SPmS). The performance metrics are calculated on both testing years 2020-2021 as one set. Since the LOADE layers increase the amount of parameters

of the 2D/3D CNN, we report the results of the one-branch 3D CNN using 323k and 499k parameters. The smaller 3D CNN has about the same amount of parameters as the 2D/3D CNN without LOADE, whereas the larger 3D CNN has more parameters than the proposed model. Due to the lack of spatial modeling, LSTM has the fewest parameters and is the fastest, but the precision is very low. ConvLSTM, the small one-branch 3D CNN, and 2D/3D CNN without LOADE and TE, which consider the spatial context, perform similar but 2D/3D CNN is the fastest approach and ConvLSTM is the slowest approach. Modulating the dynamic features conditioned on the static features (LOADE) increases all metrics. It also outperforms the large 3D CNN in all metrics and inference time. Adding TE increases all metrics when LOADE is not used, while increasing the computational cost only very little. When LOADE is used, adding TE decreases the recall but increases all other metrics. Since LOADE and TE change the dynamic features, we observe a different trade-off between recall and precision if both are used. This change is consistent over the years as shown in Table I. Nevertheless, the F1-Score, AUROC, and OA are highest if both are used.

B. Variable Importance

To assess the importance of different static variables, we present the results obtained with different combinations of static variables in Table III. For this experiment, we use 2D/3D CNN with LOADE but without TE. All dynamic variables are used in this experiment and the results are reported for the year 2019 and for the years 2020-2021 as one set. The static variables are grouped into 3 main categories: topographic variables consisting of digital elevation model (DEM) and slope, anthropogenic-related variables consisting of distance to roads or waterway and population density, and land cover variables.

From the results in Table III, we can conclude that among the 3 categories topographic variables give the best results for the years 2020-2021 when they are used without other variables. While land cover and anthropogenic-related variables provide the best results for the year 2019. Overall, all static variables are relevant and the best results are obtained when all static variables are used (last row). This is also better than using the static variables of 2 out of the 3 categories, which is reported in rows 4-6 of Table III.

C. Comparing Different Conditional Maps

While Table III shows the importance of different static variables as input to the 2D/3D CNN, we also analyze the impact of different ways to modulate the dynamic features in Table IV. For the experiments, we use the 2D/3D CNN without TE and all dynamic and static variables as input. While we use all variables, the different settings differ in the input that is fed to the LOADE layer, i.e., the static features that the modulation of the dynamic features is conditioned on.

The results of the proposed conditioning, where we use the features from the corresponding block of the static branch, are shown in the last row. In the first row, we show the results if we do not use LOADE at all, i.e., we do not use any

TABLE I

COMPARISON WITH BASELINES. THE CLASSIFICATION METRICS ARE SHOWN FOR THE YEARS 2019-2021. THE VALUES OF PRECISION, RECALL, F1-SCORE, OA, AND AUROC ARE GIVEN IN PERCENT (%). (TE) DENOTES THE ABSOLUTE TEMPORAL ENCODING.

Year 2019 (val) - 6430 samples									
Algorithm	TP(↑)	FP(↓)	TN(↑)	FN(↓)	Precision(↑)	Recall(↑)	F1-score(↑)	AUROC(↑)	OA(↑)
RF [87]	575	372	4758	725	60.72	44.23	51.18	88.54	82.94
XGBoost [88]	928	448	4682	372	67.44	71.38	69.36	92.33	87.25
LSTM [36]	968	431	4699	332	69.19	74.46	71.73	93.63	88.13
ConvLSTM [60]	867	276	4854	433	75.85	66.69	70.98	94.69	88.97
3D CNN	918	265	4865	382	77.60	70.62	73.94	94.17	89.94
2D/3D CNN	970	248	4882	330	79.64	74.62	77.05	94.52	91.01
2D/3D CNN w/ TE	905	182	4948	395	83.26	69.62	75.83	95.08	91.03
Year 2020 (test) - 6088 samples									
Algorithm	TP(↑)	FP(↓)	TN(↑)	FN(↓)	Precision(↑)	Recall(↑)	F1-score(↑)	AUROC(↑)	OA(↑)
RF [87]	750	245	4615	478	75.38	61.07	67.48	91.17	88.12
XGBoost [88]	891	322	4538	337	73.45	72.56	73.00	91.12	89.18
LSTM [36]	891	290	4570	337	75.44	72.56	73.97	93.60	89.70
ConvLSTM [60]	811	155	4705	417	83.95	66.04	73.93	94.31	90.60
3D CNN	797	160	4700	431	83.28	64.90	72.95	93.10	90.29
2D/3D CNN	841	160	4700	387	84.02	68.49	75.46	93.98	91.02
2D/3D CNN w/ TE	776	117	4743	452	86.90	63.19	73.17	94.20	90.65
Year 2021 (test) - 36732 samples									
Algorithm	TP(↑)	FP(↓)	TN(↑)	FN(↓)	Precision(↑)	Recall(↑)	F1-score(↑)	AUROC(↑)	OA(↑)
RF [87]	3264	1157	31168	1143	73.83	74.06	73.95	96.82	93.74
XGBoost [88]	3016	1345	30980	1391	69.16	68.44	68.80	95.88	92.55
LSTM [36]	3739	1359	30966	668	73.34	84.84	78.67	97.13	94.48
ConvLSTM [60]	3514	769	31556	893	82.05	79.74	80.87	97.76	95.48
3D CNN	3766	810	31515	641	82.30	85.45	83.85	98.02	96.05
2D/3D CNN	3870	757	31568	537	83.64	87.81	85.68	98.19	96.48
2D/3D CNN w/ TE	3841	416	31909	566	90.23	87.16	88.67	98.54	97.33

TABLE II

QUANTITATIVE RESULTS OF DIFFERENT DEEP LEARNING MODEL DESIGNS. THE CLASSIFICATION METRICS ARE GIVEN IN PERCENT (%). ADDITIONALLY, THE TOTAL NUMBER OF PARAMETERS (# PARAMS) AND THE INFERENCE TIME AS SAMPLES PER MILLISECOND (# SPMS) ARE PROVIDED. (TE) DENOTES THE ABSOLUTE TEMPORAL ENCODING AND LOADE THE MODULATION LAYER.

Year 2020-2021 (test)									
Algorithm	LOADE	TE	# Params(↓)	# SPmS(↑)	Precision(↑)	Recall(↑)	F1-score(↑)	AUROC(↑)	OA(↑)
LSTM [36]	×	×	30k	955±43	73.74	82.17	77.72	96.53	93.80
ConvLSTM [60]	×	×	372k	7±0	82.40	76.75	79.47	97.12	94.78
3D CNN	×	×	323k	18±1	83.93	77.48	80.58	97.15	95.08
	×	×	499k	17±1	82.47	80.98	81.72	97.15	95.23
	×	×	321k	47±0	83.35	79.98	81.63	97.11	95.26
2D/3D CNN	✓	×	413k	33±1	83.71	83.60	83.65	97.41	95.70
	×	✓	321k	47±1	83.90	84.22	84.06	97.64	95.80
	✓	✓	414k	33±2	89.65	81.93	85.62	97.78	96.38

modulation of the dynamic features. For the other rows of Table IV, we modify LOADE such that it is not conditioned on the intermediate features of the static branch as shown in Figs. 1 and 2. Instead, we condition LOADE directly on static variables. Note that we need to slightly adapt LOADE as shown in Fig. 3 since the number of static input variables C differs from the number of feature channels K at the block where LOADE is added.

As seen from Table IV, the best result is obtained when we

use the activation maps, i.e., the intermediate features, from the static branch for conditioning the modulation. However, comparable results are obtained when all static variables are directly used by the variant of LOADE shown in Fig. 4. While this variant achieves slightly higher AUROC, the variant shown in Fig. 3 achieves higher F1-score and OA. Using the static variables directly, we can analyze how the three categories of static variables impact the modulation of the dynamic features and thus the results. We can conclude that

TABLE III
PERFORMANCE METRICS FOR DIFFERENT CATEGORIES OF STATIC VARIABLES. THE VALUES ARE GIVEN IN PERCENT (%).

Static Variables	Year 2019 (val)					Year 2020-2021 (test)				
	Precision(\uparrow)	Recall(\uparrow)	F1-score(\uparrow)	AUROC(\uparrow)	OA(\uparrow)	Precision(\uparrow)	Recall(\uparrow)	F1-score(\uparrow)	AUROC(\uparrow)	OA(\uparrow)
DEM + slope	75.61	73.69	74.64	93.82	89.88	80.88	81.67	81.27	97.06	95.05
Distance to roads	77.27	76.08	76.67	94.16	90.63	81.91	74.48	78.02	96.11	94.48
Distance to waterway										
Population density										
Land cover	77.27	76.62	76.94	94.62	90.72	81.85	79.93	80.88	96.92	95.03
DEM + slope	75.09	77.00	76.03	94.09	90.19	79.64	76.89	78.24	96.69	94.37
Distance to roads										
Distance to waterway										
Population density										
DEM + slope	74.61	73.46	74.03	94.24	89.58	80.05	81.44	80.74	97.20	94.89
Land cover										
Land cover	77.52	73.23	75.32	94.52	90.30	82.63	81.12	81.87	96.98	95.27
Distance to roads										
Distance to waterway										
Population density										
All static variables	79.64	74.62	77.05	94.52	91.01	83.71	83.60	83.65	97.41	95.70

TABLE IV
IMPACT OF DIFFERENT CONDITIONAL MAPS ON THE FEATURE MODULATION. THE EVALUATION METRICS ARE GIVEN IN PERCENT (%).

Conditional Map	Year 2019 (val)					Year 2020-2021 (test)				
	Precision(\uparrow)	Recall(\uparrow)	F1-score(\uparrow)	AUROC(\uparrow)	OA(\uparrow)	Precision(\uparrow)	Recall(\uparrow)	F1-score(\uparrow)	AUROC(\uparrow)	OA(\uparrow)
—	75.68	62.23	68.30	93.38	88.32	83.35	79.98	81.63	97.11	95.26
DEM + slope	70.84	71.00	70.92	92.77	88.23	76.90	79.45	78.15	96.16	94.15
Distance to roads	73.83	76.15	74.97	93.74	89.72	77.98	76.63	77.30	96.22	94.08
Distance to waterway										
Population density										
Land cover	79.05	72.00	75.36	94.58	90.48	81.53	75.19	78.23	96.80	94.49
All static variables	77.12	74.92	76.00	94.95	90.44	81.05	84.08	82.54	97.55	95.32
Activation maps (Static branch)	79.64	74.62	77.05	94.52	91.01	83.71	83.60	83.65	97.41	95.70

the modulation of the dynamic features is very sensitive to its condition. For the year 2019, all three categories (rows 2-4) improve the results compared to the setup without feature modulation (first row). For the years 2020-2021, this is not the case and only the combination of all static variables (row 5) leads to an improvement. The reason is the mismatch between C and K^i . Compared to the other categories, land cover has the highest number of variables per pixels ($C=10$) and shows the best performance. This indicates that conditioning the modulation of the dynamic features on the intermediate features of the static branch is a more practical approach than conditioning the modulation on the static variables directly, which seems to be sensitive to the number of variables.

D. Qualitative Results

Predicted wildfire danger-susceptibility maps are depicted in Figs. 6, 7, and 8. We take input from the 1st and 2nd days of three consecutive months in summer (June, July, and August) and predict for the 2nd and 3rd days of each month. We end up with around 500k pixels (samples) per day. The output

from the deep learning models (LSTM, ConvLSTM, Ours) is a probability $Y \in [0, 1]$. In addition, we visualize the predicted maps produced by FWI with the provided spatial resolution $8 \text{ km} \times 8 \text{ km}$. The output of FWI is clipped to the range $[0, 50]$ [13]. The ignition points of large wildfires at those days are represented as black circles on the map. The first observation is that regardless of the coarse resolution of FWI, the predicted maps produced by the deep learning models are more reliable. While FWI relies on meteorological observations and models functional relationships, the results show that the modeled functional relationships are insufficient and do not reflect the complexity of the problem of forecasting wildfire. We also find that our proposed model with TE discards spots that result in a high false positive error rate while it keeps extreme ones (cf. the results for July in 2020 and 2021). Another important observation is that the LSTM model, which does not account for the spatial context, tends to produce heterogeneous predictions where neighboring pixels often have very different wildfire danger probabilities. Consequently, it generates many false positives. In contrast, our proposed model and ConvLSTM

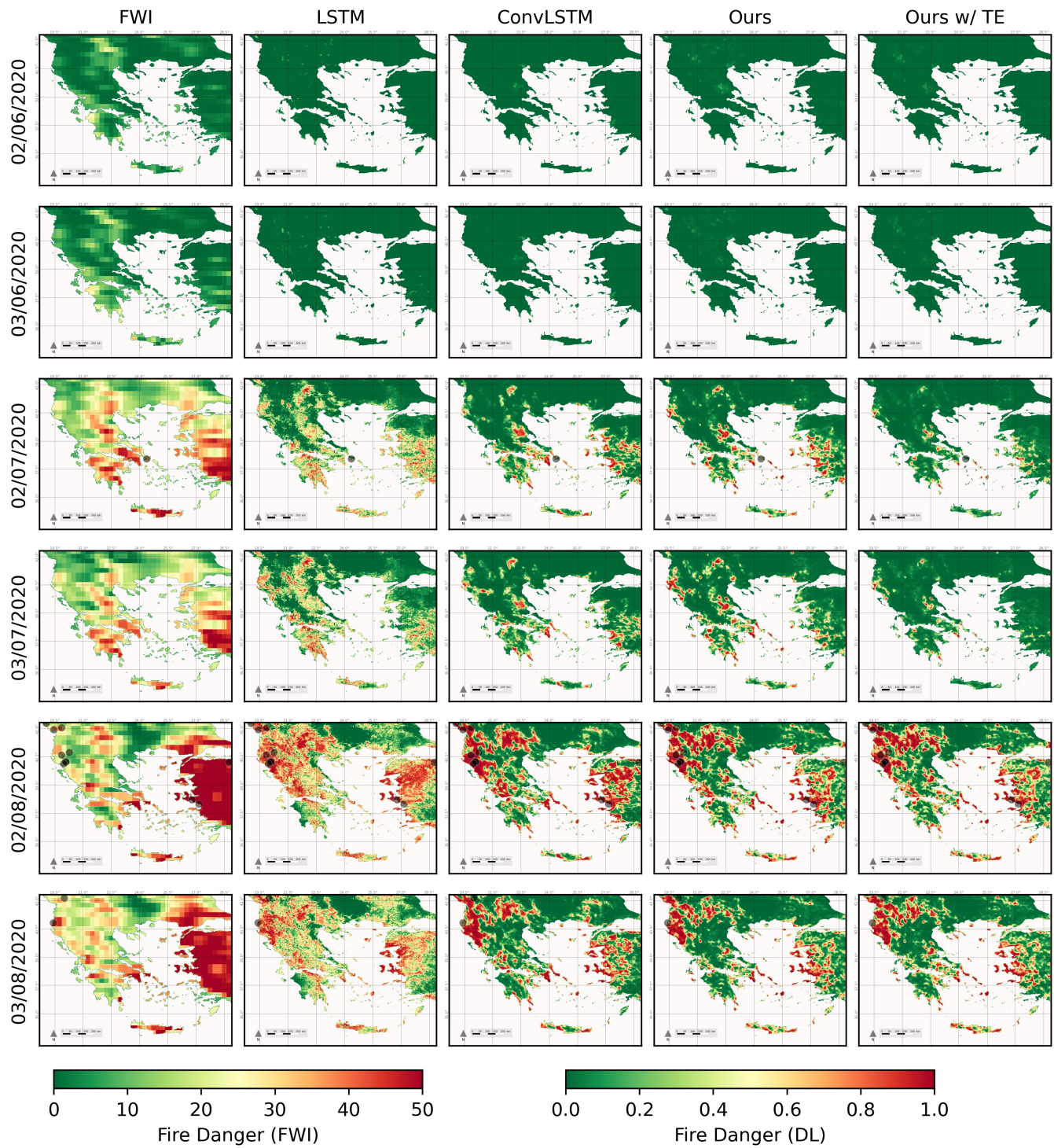


Fig. 6. Qualitative results for 6 days during the wildfire season in year 2020. The black circles represent an ignition of a large wildfire on that day. (TE) denotes absolute temporal encoding.

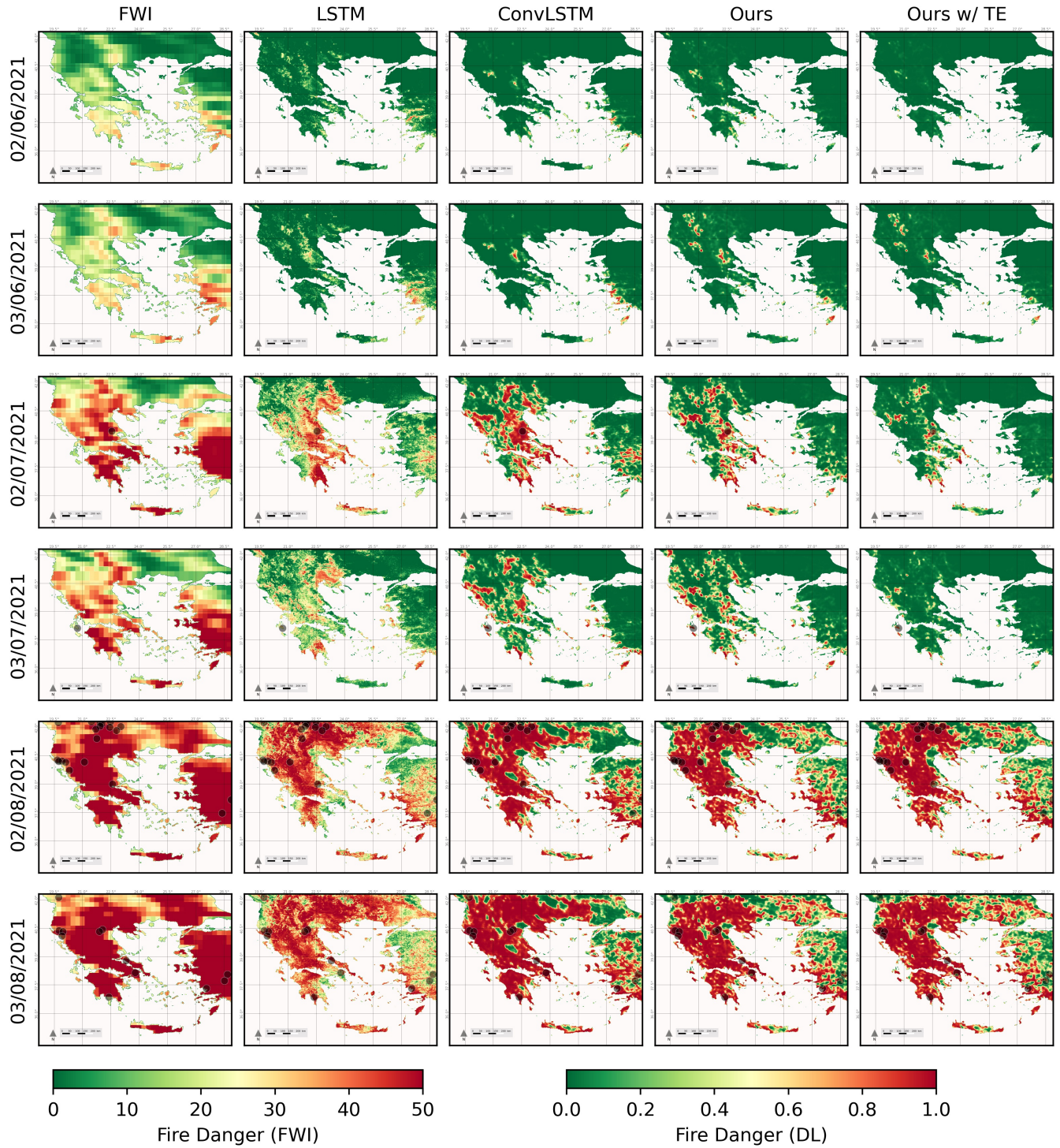


Fig. 7. Qualitative results for 6 days during the wildfire season in the extreme year 2021. The black circles represent an ignition of a large wildfire on that day. (TE) denotes absolute temporal encoding.

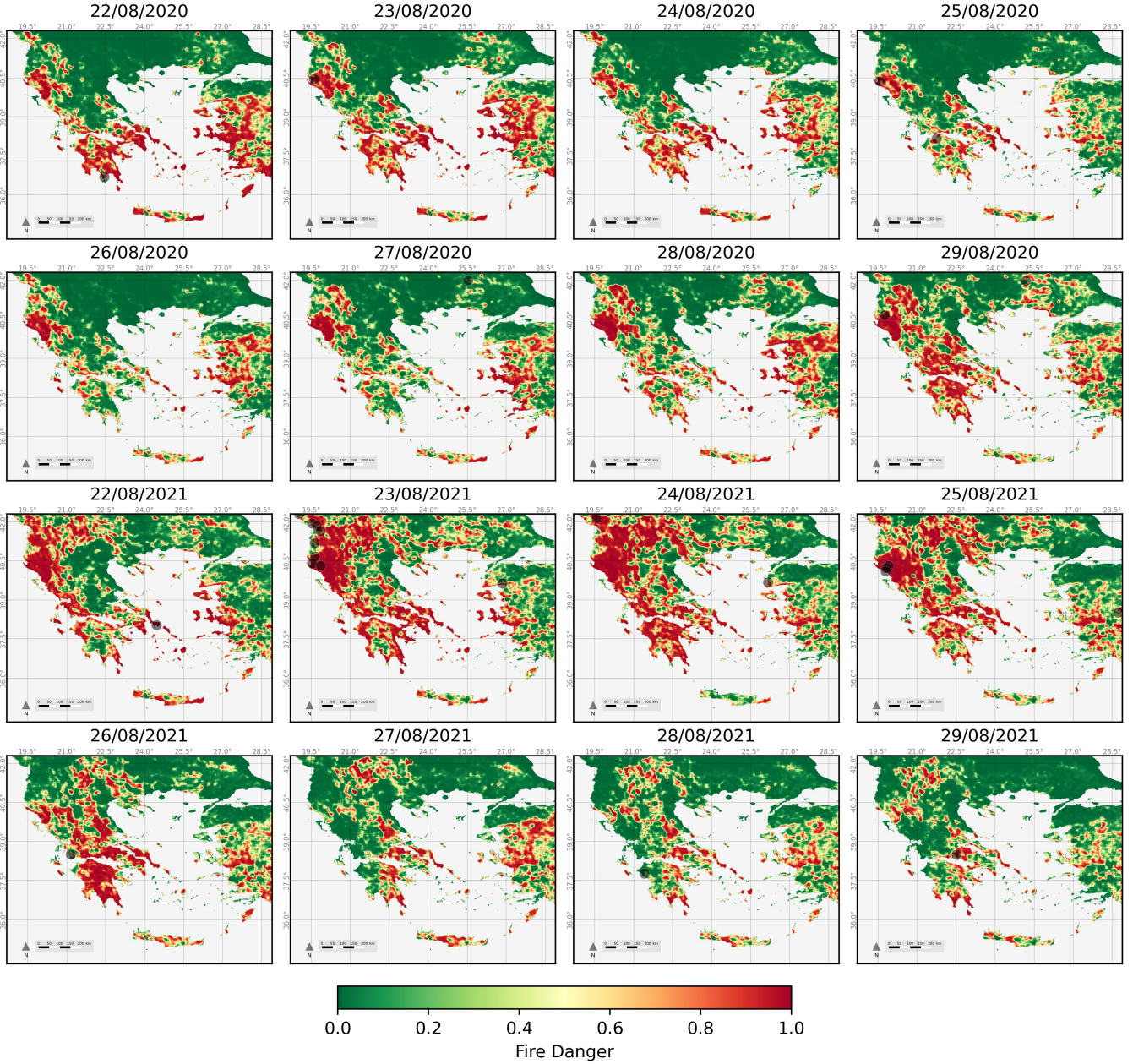


Fig. 8. Predictions for 8 consecutive days in August. The upper two rows show the results for the year 2020 and the last two rows show the results for the extreme year 2021. The maps are produced by the proposed 2D/3D CNN with absolute temporal encoding. The black circles represent an ignition of a large wildfire on that day.

produce more homogeneous and clustered predictions. The respective performance metrics for Fig. 6 and 7 are provided in Table V.

VI. ABLATION STUDY

We finally evaluate two additional aspects. In Section VI-A, we analyze at which blocks of the proposed 2D/3D CNN LOADE is best added and the impact of the absolute temporal encoding with respect to the number of negative samples in Section VI-B.

A. LOADE Position in the Model

As shown in Fig. 1, the proposed network has three blocks and we add LOADE to the first and second block. We evaluate in Table VI different configurations where we add LOADE only to the first or to all three blocks. The results are reported without TE. If we add LOADE only to the first block, the performance increases for the year 2019 but not for the years 2020-2021 compared to our model without LOADE (first row). When adding LOADE to the first two blocks, we observe a consistent improvement for all years. For the year 2019, Precision, Recall, F1-score, and AUROC are improved by +3.96%, +12.39%, +8.75%, and +1.14%, respectively, and

TABLE V

RECALL (%) METRIC PER CLASS FOR FIGURES 5 AND 6. (P) DENOTES THE POSITIVE CLASS AND (N) THE NEGATIVE ONE. THE NUMBER OF POSITIVE SAMPLES IS SHOWN BELOW THE DATE. THIS IS EQUIVALENT TO THE AREA (KM²) THAT WAS BURNED BY LARGE WILDFIRES AT THAT DAY.

# Positive samples	02/06/2020 0		03/06/2020 0		02/07/2020 2		03/07/2020 0		02/08/2020 71		03/08/2020 25	
Algorithm	P	N	P	N	P	N	P	N	P	N	P	N
LSTM [36]	-	99.98	-	99.96	00.00	81.41	-	82.37	87.32	48.93	88.00	56.23
ConvLSTM [60]	-	100.00	-	100.00	00.00	89.72	-	92.46	92.96	65.09	80.00	72.52
2D/3D CNN	-	100.00	-	99.99	100.00	89.51	-	90.33	73.24	66.74	80.00	76.17
2D/3D CNN w/ TE	-	100.00	-	100.00	00.00	96.81	-	97.92	78.87	65.68	80.00	74.32

# Positive samples	02/06/2021 0		03/06/2021 0		02/07/2021 36		03/07/2021 22		02/08/2021 679		03/08/2021 1417	
Algorithm	P	N	P	N	P	N	P	N	P	N	P	N
LSTM [36]	-	98.23	-	96.44	100.00	70.58	68.18	83.14	82.03	32.54	93.30	23.88
ConvLSTM [60]	-	99.11	-	98.25	100.00	75.53	100.00	87.42	71.87	35.66	87.01	28.28
2D/3D CNN	-	99.38	-	98.08	100.00	84.36	100.00	88.97	83.80	39.17	99.29	33.75
2D/3D CNN w/ TE	-	99.91	-	98.95	100.00	94.77	100.00	98.61	85.13	36.67	99.36	31.67

TABLE VI

ABLATION STUDY OF DIFFERENT POSITION CHOICES FOR THE LOADE LAYER. ALL CLASSIFICATION METRICS ARE GIVEN IN PERCENT (%).

Year 2019 (val)							
Block			Precision(↑)	Recall(↑)	F1-score(↑)	AUROC(↑)	
1 st	2 nd	3 rd					
×	×	×	75.68	62.23	68.30	93.38	
✓	×	×	76.90	75.54	76.21	94.40	
✓	✓	×	79.64	74.62	77.05	94.52	
✓	✓	✓	73.92	70.85	72.35	93.68	

Year 2020-2021 (test)							
Block			Precision(↑)	Recall(↑)	F1-score(↑)	AUROC(↑)	
1 st	2 nd	3 rd					
×	×	×	83.35	79.98	81.63	97.11	
✓	×	×	80.90	78.72	79.80	97.22	
✓	✓	×	83.71	83.60	83.65	97.41	
✓	✓	✓	79.77	81.30	80.52	96.92	

by +0.36%, +3.62%, +2.02%, and +0.30% for the years 2020-2021, respectively. Adding LOADE to all three blocks performs worse than adding LOADE only to the first two blocks. This is due to the decrease of spatial resolution after each block by the pooling layers. In the third block the spatial resolution is too coarse for a location-specific modulation of the dynamic features.

B. Absolute Temporal Encoding

As we have seen in Table I, absolute temporal encoding (TE) increases precision at the cost of lower recall. Depending on the use of the wildfire forecasting, recall or precision are more important. The precision also depends on the amount of negative samples. In order to show that TE gives consistently a higher precision, we varied the number of negative samples. In this experiment, we test on all positive samples in the test set (years 2020-2021) and gradually increase the number of

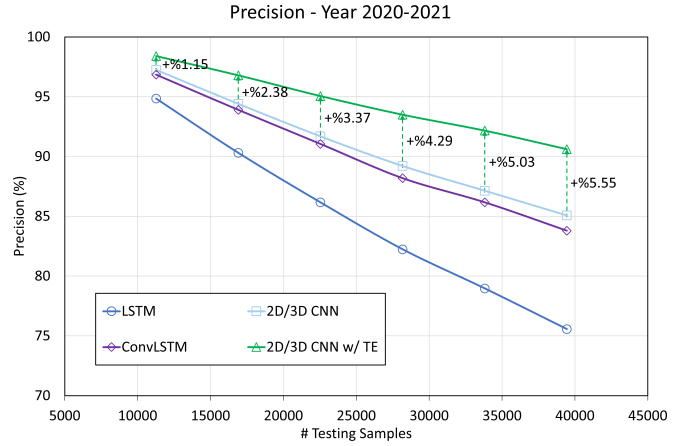


Fig. 9. Impact of the number of testing samples on the precision. (TE) denotes the absolute temporal encoding.

negative ones. As shown in Fig. 9, we start with a setup where the number of negative samples is equal to the number of positive samples, i.e., 5635 positive and 5635 negative samples. We then increase the number of negative samples. Since the number of negative samples increases, the precision decreases for all methods. Note that the recall does not change since the number of positive samples remains the same. As already observed in Table I, LSTM has a very low precision. 2D/3D CNN with LOADE has in all settings a higher precision than ConvLSTM and a much higher recall as shown in Table I. While adding TE decreases recall, it improves the precision substantially and the improvement increases when the number of negative samples increases. While other metrics like F1-score or AUROC combine precision and recall in a single measure, depending on the application a higher recall or a higher precision might be more important. If precision is more important, TE is very useful. If recall is more important, TE should not be used. We also point out that TE encodes only the day of the year since the dataset has a relatively small spatial extension (10.2°Lon × 8°Lat). In case of larger datasets at continental scale, a consideration of the spatial

location for the encoding would also become relevant as biogeographical regions occur [69], which are characterized by different climate variabilities and anthropogenic drivers over time.

VII. CONCLUSION

In this work, we proposed a new deep learning approach for wildfire danger forecasting. In contrast to previous works, we handle spatial (static) and spatio-temporal (dynamic) variables differently. Our model processes the spatial and spatio-temporal variables in two separated 2D/3D CNN branches to learn static and dynamic feature vectors. Moreover, we have introduced the Location-aware Adaptive Denormalization layer, which modulates the activation maps in the dynamic branch conditionally on their respective static features to address the causal effect of static features on dynamic features. We furthermore integrated an absolute time encoding into the model. By encoding the calendar time, we make the model explicitly aware of the forecasting day. While the time encoding reduces the recall, it substantially increases the precision. We conducted our experiments on the FireCube dataset and demonstrated the effectiveness of our approach compared to several baselines in terms of Precision, F1-score, AUROC, and OA. We believe that the proposed approach of dealing with spatial and spatial-temporal variables is also highly relevant for other remote sensing applications. While we demonstrated a substantial improvement compared to previous works for wildfire forecasting, it remains a challenging task that requires more research efforts. This requires further developments and improvements of the approaches as well as larger datasets at continental scale with a standardized evaluation framework.

ACKNOWLEDGMENTS

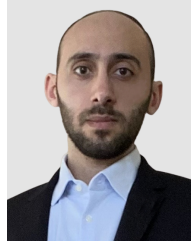
We would like to thank Ioannis Prapas and Spyros Kondylatos for providing the data cube.

REFERENCES

- [1] L. Ren, P. Arkin, T. M. Smith, and S. S. Shen, "Global precipitation trends in 1900–2005 from a reconstruction and coupled model simulations," *Journal of Geophysical Research: Atmospheres*, vol. 118, no. 4, pp. 1679–1689, 2013. [Online]. Available: <https://agupubs.onlinelibrary.wiley.com/doi/abs/10.1002/jgrd.50212>
- [2] A. M. Lausier and S. Jain, "Overlooked trends in observed global annual precipitation reveal underestimated risks," *Scientific reports*, vol. 8, no. 1, pp. 1–7, 2018.
- [3] S. Perkins-Kirkpatrick and S. Lewis, "Increasing trends in regional heatwaves," *Nature communications*, vol. 11, no. 1, pp. 1–8, 2020.
- [4] R. Samuels, A. Hochman, A. Baharad, A. Givati, Y. Levi, Y. Yosef, H. Saaroni, B. Ziv, T. Harpaz, and P. Alpert, "Evaluation and projection of extreme precipitation indices in the eastern mediterranean based on cmip5 multi-model ensemble," *International Journal of Climatology*, vol. 38, no. 5, pp. 2280–2297, 2018.
- [5] G. Zittis, P. Hadjinicolaou, M. Klagidou, Y. Proestos, and J. Lelieveld, "A multi-model, multi-scenario, and multi-domain analysis of regional climate projections for the mediterranean," *Regional Environmental Change*, vol. 19, no. 8, pp. 2621–2635, 2019.
- [6] M. J. Barcikowska, S. B. Kapnick, L. Krishnamurthy, S. Russo, A. Cherchi, and C. K. Folland, "Changes in the future summer mediterranean climate: contribution of teleconnections and local factors," *Earth System Dynamics*, vol. 11, no. 1, pp. 161–181, 2020. [Online]. Available: <https://esd.copernicus.org/articles/11/161/2020/>
- [7] A. Hochman, F. Marra, G. Messori, J. G. Pinto, S. Raveh-Rubin, Y. Yosef, and G. Zittis, "Extreme weather and societal impacts in the eastern mediterranean," *Earth System Dynamics*, vol. 13, no. 2, pp. 749–777, 2022. [Online]. Available: <https://esd.copernicus.org/articles/13/749/2022/>
- [8] M. P. Thompson, Y. Wei, D. E. Calkin, C. D. O'Connor, C. J. Dunn, N. M. Anderson, and J. S. Hogland, "Risk management and analytics in wildfire response," *Current Forestry Reports*, vol. 5, no. 4, pp. 226–239, 2019.
- [9] S. C. P. Coogan, F. Robinne, P. Jain, and M. D. Flannigan, "Scientists' warning on wildfire — a canadian perspective," *Canadian Journal of Forest Research*, 2019.
- [10] F. Moreira, D. Ascoli, H. Safford, M. A. Adams, J. M. Moreno, J. M. C. Pereira, F. X. Catry, J. Armesto, W. Bond, M. E. González, T. Curt, N. Koutsias, L. McCaw, O. Price, J. G. Pausas, E. Rigolot, S. Stephens, C. Tavsanoglu, V. R. Vallejo, B. W. V. Wilgen, G. Xanthopoulos, and P. M. Fernandes, "Wildfire management in mediterranean-type regions: paradigm change needed," *Environmental Research Letters*, vol. 15, no. 1, p. 011001, jan 2020. [Online]. Available: <https://dx.doi.org/10.1088/1748-9326/ab541e>
- [11] P. Jain, S. C. Coogan, S. G. Subramanian, M. Crowley, S. Taylor, and M. D. Flannigan, "A review of machine learning applications in wildfire science and management," *Environmental Reviews*, vol. 28, no. 4, pp. 478–505, 2020.
- [12] D. Fornacca, G. Ren, and W. Xiao, "Performance of three modis fire products (mcd45a1, mcd64a1, mcd14ml), and esa fire_cci in a mountainous area of northwest yunnan, china, characterized by frequent small fires," *Remote Sensing*, vol. 9, no. 11, p. 1131, 2017.
- [13] S. Kondylatos, I. Prapas, M. Ronco, I. Papoutsis, G. Camps-Valls, M. Piles, M.-Á. Fernández-Torres, and N. Carvalhais, "Wildfire danger prediction and understanding with deep learning," *Geophysical Research Letters*, vol. 49, no. 17, p. e2022GL099368, 2022. [Online]. Available: <https://agupubs.onlinelibrary.wiley.com/doi/abs/10.1029/2022GL099368>
- [14] S. Hanson, A. Arneeth, S. P. Harrison, D. I. Kelley, I. C. Prentice, S. S. Rabin, S. Archibald, F. Mouillot, S. R. Arnold, P. Artaxo *et al.*, "The status and challenge of global fire modelling," *Biogeosciences*, vol. 13, no. 11, pp. 3359–3375, 2016.
- [15] M. Reichstein, G. Camps-Valls, B. Stevens, M. Jung, J. Denzler, N. Carvalhais *et al.*, "Deep learning and process understanding for data-driven earth system science," *Nature*, vol. 566, no. 7743, pp. 195–204, 2019.
- [16] I. Prapas, S. Kondylatos, I. Papoutsis, G. Camps-Valls, M. Ronco, M.-Á. Fernández-Torres, M. P. Guillem, and N. Carvalhais, "Deep learning methods for daily wildfire danger forecasting," 2021. [Online]. Available: <https://arxiv.org/abs/2111.02736>
- [17] I. Prapas, S. Kondylatos, and I. Papoutsis, "FireCube: A Daily Datacube for the Modeling and Analysis of Wildfires in Greece," May 2022. [Online]. Available: <https://doi.org/10.5281/zenodo.6475592>
- [18] M. C. Iban and A. Sekertekin, "Machine learning based wildfire susceptibility mapping using remotely sensed fire data and gis: A case study of adana and mersin provinces, turkey," *Ecological Informatics*, vol. 69, p. 101647, 2022. [Online]. Available: <https://www.sciencedirect.com/science/article/pii/S1574954122000966>
- [19] T. Jiang, S. K. Bendre, H. Lyu, and J. Luo, "From static to dynamic prediction: Wildfire risk assessment based on multiple environmental factors," in *2021 IEEE International Conference on Big Data (Big Data)*, 2021, pp. 4877–4886.
- [20] H. V. Le, D. A. Hoang, C. T. Tran, P. Q. Nguyen, V. H. T. Tran, N. D. Hoang, M. Amiri, T. P. T. Ngo, H. V. Nhu, T. V. Hoang, and D. Tien Bui, "A new approach of deep neural computing for spatial prediction of wildfire danger at tropical climate areas," *Ecological Informatics*, vol. 63, p. 101300, 2021. [Online]. Available: <https://www.sciencedirect.com/science/article/pii/S1574954121000911>
- [21] G. Zhang, M. Wang, and K. Liu, "Forest fire susceptibility modeling using a convolutional neural network for yunnan province of china," *International Journal of Disaster Risk Science*, vol. 10, no. 3, pp. 386–403, 2019.
- [22] —, "Deep neural networks for global wildfire susceptibility modelling," *Ecological Indicators*, vol. 127, p. 107735, 2021. [Online]. Available: <https://www.sciencedirect.com/science/article/pii/S1470160X21004003>
- [23] A. Bjănes, R. De La Fuente, and P. Mena, "A deep learning ensemble model for wildfire susceptibility mapping," *Ecological Informatics*, vol. 65, p. 101397, 2021. [Online]. Available: <https://www.sciencedirect.com/science/article/pii/S1574954121001886>

- [24] J. R. Bergado, C. Persello, K. Reinke, and A. Stein, "Predicting wildfire burns from big geodata using deep learning," *Safety science*, vol. 140, p. 105276, 2021.
- [25] F. Huot, R. L. Hu, N. Goyal, T. Sankar, M. Ihme, and Y.-F. Chen, "Next day wildfire spread: A machine learning dataset to predict wildfire spreading from remote-sensing data," *IEEE Transactions on Geoscience and Remote Sensing*, vol. 60, pp. 1–13, 2022.
- [26] I. Prapas, A. Ahuja, S. Kondylatos, I. Karasante, L. Alonso, E. Panagiotou, C. Davalas, D. Michail, N. Carvahais, and I. Papoutsis, "Deep learning for global wildfire forecasting," in *NeurIPS 2022 Workshop on Tackling Climate Change with Machine Learning*, 2022. [Online]. Available: <https://www.climatechange.ai/papers/neurips2022/52>
- [27] Q. Zhao, Y. Ma, S. Lyu, and L. Chen, "Embedded self-distillation in compact multibranch ensemble network for remote sensing scene classification," *IEEE Transactions on Geoscience and Remote Sensing*, vol. 60, pp. 1–15, 2022.
- [28] R. Gaetano, D. Ienco, K. Ose, and R. Cresson, "A two-branch cnn architecture for land cover classification of pan and ms imagery," *Remote Sensing*, vol. 10, no. 11, 2018. [Online]. Available: <https://www.mdpi.com/2072-4292/10/11/1746>
- [29] Y. Tan, S. Xiong, and P. Yan, "Multi-branch convolutional neural network for built-up area extraction from remote sensing image," *Neurocomputing*, vol. 396, pp. 358–374, 2020. [Online]. Available: <https://www.sciencedirect.com/science/article/pii/S0925231219309208>
- [30] Y. Xu, L. Zhang, B. Du, and F. Zhang, "Spectral-spatial unified networks for hyperspectral image classification," *IEEE Transactions on Geoscience and Remote Sensing*, vol. 56, no. 10, pp. 5893–5909, 2018.
- [31] Y. Shen, L. Xiao, J. Chen, and D. Pan, "A spectral-spatial domain-specific convolutional deep extreme learning machine for supervised hyperspectral image classification," *IEEE Access*, vol. 7, pp. 132 240–132 252, 2019.
- [32] X. Liu, C. Deng, J. Chanussot, D. Hong, and B. Zhao, "Stfnnet: A two-stream convolutional neural network for spatiotemporal image fusion," *IEEE Transactions on Geoscience and Remote Sensing*, vol. 57, no. 9, pp. 6552–6564, 2019.
- [33] C. Gan, X. Yan, Y. Wu, and Z. Zhang, "A two-branch convolution residual network for image compressive sensing," *IEEE Access*, vol. 8, pp. 1705–1714, 2020.
- [34] Y. Tang, X. Xie, and Y. Yu, "Hyperspectral classification of two-branch joint networks based on gaussian pyramid multiscale and wavelet transform," *IEEE Access*, vol. 10, pp. 56 876–56 887, 2022.
- [35] Z. Zhong, J. Li, L. Ma, H. Jiang, and H. Zhao, "Deep residual networks for hyperspectral image classification," in *2017 IEEE International Geoscience and Remote Sensing Symposium (IGARSS)*, 2017, pp. 1824–1827.
- [36] S. Hochreiter and J. Schmidhuber, "Long short-term memory," *Neural computation*, vol. 9, pp. 1735–80, 12 1997.
- [37] Y. Zheng, S. Liu, Q. Du, H. Zhao, X. Tong, and M. Dalponte, "A novel multitemporal deep fusion network (mdfn) for short-term multitemporal hr images classification," *IEEE Journal of Selected Topics in Applied Earth Observations and Remote Sensing*, vol. 14, pp. 10 691–10 704, 2021.
- [38] R. Li, S. Zheng, C. Duan, Y. Yang, and X. Wang, "Classification of hyperspectral image based on double-branch dual-attention mechanism network," *Remote Sensing*, vol. 12, no. 3, 2020. [Online]. Available: <https://www.mdpi.com/2072-4292/12/3/582>
- [39] Z. Zhu, Y. Tao, and X. Luo, "Hcnnet: A hybrid convolutional neural network for spatiotemporal image fusion," *IEEE Transactions on Geoscience and Remote Sensing*, vol. 60, pp. 1–16, 2022.
- [40] Z. Deng, Y. Wang, B. Zhang, L. Li, J. Wang, L. Bian, and C. Yang, "A triple-path spectral-spatial network with interleave-attention for hyperspectral image classification," *IEEE Journal of Selected Topics in Applied Earth Observations and Remote Sensing*, vol. 15, pp. 5906–5923, 2022.
- [41] S. Ioffe and C. Szegedy, "Batch normalization: Accelerating deep network training by reducing internal covariate shift," in *International conference on machine learning*. PMLR, 2015, pp. 448–456.
- [42] Y. Wu and K. He, "Group normalization," in *Proceedings of the European conference on computer vision (ECCV)*, 2018, pp. 3–19.
- [43] D. Ulyanov, A. Vedaldi, and V. S. Lempitsky, "Instance normalization: The missing ingredient for fast stylization," *ArXiv*, vol. abs/1607.08022, 2016.
- [44] J. Ba, J. R. Kiros, and G. E. Hinton, "Layer normalization," *ArXiv*, vol. abs/1607.06450, 2016.
- [45] T. Park, M.-Y. Liu, T.-C. Wang, and J.-Y. Zhu, "Semantic image synthesis with spatially-adaptive normalization," in *2019 IEEE/CVF Conference on Computer Vision and Pattern Recognition (CVPR)*, 2019, pp. 2332–2341.
- [46] X. Wang, K. Yu, C. Dong, and C. Change Loy, "Recovering realistic texture in image super-resolution by deep spatial feature transform," in *2018 IEEE/CVF Conference on Computer Vision and Pattern Recognition*, 2018, pp. 606–615.
- [47] X. Huang and S. Belongie, "Arbitrary style transfer in real-time with adaptive instance normalization," in *Proceedings of the IEEE international conference on computer vision*, 2017, pp. 1501–1510.
- [48] J. Ling, H. Xue, L. Song, R. Xie, and X. Gu, "Region-aware adaptive instance normalization for image harmonization," in *2021 IEEE/CVF Conference on Computer Vision and Pattern Recognition (CVPR)*, 2021, pp. 9357–9366.
- [49] N. van Noord and E. Postma, "A learned representation of artist-specific colourisation," in *Proceedings of the IEEE International Conference on Computer Vision (ICCV) Workshops*, Oct 2017.
- [50] P. Zhu, R. Abdal, Y. Qin, and P. Wonka, "Sean: Image synthesis with semantic region-adaptive normalization," in *2020 IEEE/CVF Conference on Computer Vision and Pattern Recognition (CVPR)*, 2020, pp. 5103–5112.
- [51] Z. Tan, D. Chen, Q. Chu, M. Chai, J. Liao, M. He, L. Yuan, G. Hua, and N. Yu, "Efficient semantic image synthesis via class-adaptive normalization," *IEEE Transactions on Pattern Analysis and Machine Intelligence*, vol. 44, no. 9, pp. 4852–4866, 2022.
- [52] Z. Lv, X. Li, X. Li, F. Li, T. Lin, D. He, and W. Zuo, "Learning semantic person image generation by region-adaptive normalization," in *2021 IEEE/CVF Conference on Computer Vision and Pattern Recognition (CVPR)*, 2021, pp. 10 801–10 810.
- [53] Y. Lyu, P. Chen, J. Sun, X. Wang, J. Dong, and T. Tan, "Detailed region-adaptive normalization for heavy makeup transfer," *arXiv preprint arXiv:2109.14525*, 2021.
- [54] K. Jakoeel, L. Efraim, and T. R. Shaham, "Gans spatial control via inference-time adaptive normalization," in *2022 IEEE/CVF Winter Conference on Applications of Computer Vision (WACV)*, 2022, pp. 31–40.
- [55] T. Chen, M. Lucic, N. Houlsby, and S. Gelly, "On self modulation for generative adversarial networks," 2019. [Online]. Available: <https://openreview.net/forum?id=Hk15aoR5tm>
- [56] X. Huang and S. J. Belongie, "Arbitrary style transfer in real-time with adaptive instance normalization," *2017 IEEE International Conference on Computer Vision (ICCV)*, pp. 1510–1519, 2017.
- [57] V. Sushko, E. Schönfeld, D. Zhang, J. Gall, B. Schiele, and A. Khoreva, "Oasis: Only adversarial supervision for semantic image synthesis," *International Journal of Computer Vision*, 2022.
- [58] S. Li, M.-M. Cheng, and J. Gall, in *Dual Pyramid Generative Adversarial Networks for Semantic Image Synthesis*, 2022.
- [59] J. Marín and S. Escalera, "Ssgan: Satellite style and structure generative adversarial networks," *Remote Sensing*, vol. 13, no. 19, 2021. [Online]. Available: <https://www.mdpi.com/2072-4292/13/19/3984>
- [60] X. Shi, Z. Chen, H. Wang, D.-Y. Yeung, W.-K. Wong, and W.-c. Woo, "Convolutional lstm network: A machine learning approach for precipitation nowcasting," *Advances in neural information processing systems*, vol. 28, 2015.
- [61] M. Rußwurm and M. Körner, "Multi-temporal land cover classification with sequential recurrent encoders," *ISPRS International Journal of Geo-Information*, vol. 7, no. 4, 2018. [Online]. Available: <https://www.mdpi.com/2220-9964/7/4/129>
- [62] C. Pelletier, G. I. Webb, and F. Petitjean, "Temporal convolutional neural network for the classification of satellite image time series," *Remote Sensing*, vol. 11, no. 5, p. 523, 2019, <https://www.mdpi.com/2072-4292/11/5/523>.
- [63] W. R. Moskolai, W. Abdou, A. Dipanda, and Kolyang, "Application of deep learning architectures for satellite image time series prediction: A review," *Remote Sensing*, vol. 13, no. 23, 2021. [Online]. Available: <https://www.mdpi.com/2072-4292/13/23/4822>
- [64] A. Vaswani, N. Shazeer, N. Parmar, J. Uszkoreit, L. Jones, A. N. Gomez, Ł. Kaiser, and I. Polosukhin, "Attention is all you need," *Advances in neural information processing systems*, vol. 30, 2017.
- [65] V. S. F. Garnot, L. Landrieu, S. Giordano, and N. Chehata, "Satellite image time series classification with pixel-set encoders and temporal self-attention," in *Proceedings of the IEEE/CVF Conference on Computer Vision and Pattern Recognition*, 2020, pp. 12 325–12 334.
- [66] V. S. F. Garnot and L. Landrieu, "Lightweight temporal self-attention for classifying satellite images time series," in *Advanced Analytics and Learning on Temporal Data*, V. Lemaire, S. Malinowski, A. Bagnall, T. Guyet, R. Tavenard, and G. Ifrim, Eds. Cham: Springer International Publishing, 2020, pp. 171–181.

- [67] V. S. Fare Garnot and L. Landrieu, "Panoptic segmentation of satellite image time series with convolutional temporal attention networks," in *2021 IEEE/CVF International Conference on Computer Vision (ICCV)*, 2021, pp. 4852–4861.
- [68] L. Drees, I. Weber, M. Rußwurm, and R. Roscher, "Time dependent image generation of plants from incomplete sequences with cnn-transformer," in *DAGM German Conference on Pattern Recognition*. Springer, 2022, pp. 495–510.
- [69] J. Nyborg, C. Pelletier, S. Lefèvre, and I. Assent, "Timematch: Unsupervised cross-region adaptation by temporal shift estimation," *ISPRS Journal of Photogrammetry and Remote Sensing*, vol. 188, pp. 301–313, 2022. [Online]. Available: <https://www.sciencedirect.com/science/article/pii/S0924271622001216>
- [70] J. Nyborg, C. Pelletier, and I. Assent, "Generalized classification of satellite image time series with thermal positional encoding," in *2022 IEEE/CVF Conference on Computer Vision and Pattern Recognition Workshops (CVPRW)*, 2022, pp. 1391–1401.
- [71] J. Muñoz Sabater, E. Dutra, A. Agustí-Panareda, C. Albergel, G. Arduini, G. Balsamo, S. Boussetta, M. Choulga, S. Harrigan, H. Hersbach, B. Martens, D. G. Miralles, M. Piles, N. J. Rodríguez-Fernández, E. Zsoter, C. Buontempo, and J.-N. Thépaut, "Era5-land: a state-of-the-art global reanalysis dataset for land applications," *Earth System Science Data*, vol. 13, no. 9, pp. 4349–4383, 2021. [Online]. Available: <https://essd.copernicus.org/articles/13/4349/2021/>
- [72] K. Didan, "Mod13a2 modis/terra vegetation indices 16-day 13 global 1km sin grid v006 [data set]. nasa eosdis land processes daac," 2015. [Online]. Available: <https://doi.org/10.5067/MODIS/MOD13A2.006>
- [73] Z. Wan, S. Hook, and G. Hulley, "Mod11a2 modis/terra land surface temperature/emissivity 8-day 13 global 1km sin grid v006," 2015. [Online]. Available: <https://doi.org/10.5067/MODIS/MOD11A2.006>
- [74] A. Bashfield and A. Keim, "Continent-wide dem creation for the european union," in *34th International Symposium on Remote Sensing of Environment. The GEOSS Era: Towards Operational Environmental Monitoring*. Sydney, Australia, 2011, pp. 10–15.
- [75] A. J. Tatem, "Worldpop, open data for spatial demography," *Scientific data*, vol. 4, no. 1, pp. 1–4, 2017.
- [76] J. San-Miguel-Ayanz, E. Schulte, G. Schmuck, and A. Camia, "The european forest fire information system in the context of environmental policies of the european union," *Forest Policy and Economics*, vol. 29, pp. 19–25, 2013, the FIRE PARADOX project: Setting the basis for a shift in the forest fire policies in Europe. [Online]. Available: <https://www.sciencedirect.com/science/article/pii/S138993411200127X>
- [77] L. Giglio, W. Schroeder, and C. O. Justice, "The collection 6 modis active fire detection algorithm and fire products," *Remote Sensing of Environment*, vol. 178, pp. 31–41, 2016. [Online]. Available: <https://www.sciencedirect.com/science/article/pii/S0034425716300827>
- [78] G. Büttner, *CORINE Land Cover and Land Cover Change Products*. Dordrecht: Springer Netherlands, 2014, pp. 55–74. [Online]. Available: https://doi.org/10.1007/978-94-007-7969-3_5
- [79] D. Steinfeld, *Calculation of indices for forest fire risk assessment in weather and climate data*, 2022. [Online]. Available: <https://github.com/steidani/FireDanger>
- [80] T. M. Giannaros, G. Papavasileiou, K. Lagouvardos, V. Kotroni, S. Dafis, A. Karagiannidis, and E. Dragozi, "Meteorological analysis of the 2021 extreme wildfires in greece: Lessons learned and implications for early warning of the potential for pyroconvection," *Atmosphere*, vol. 13, no. 3, 2022. [Online]. Available: <https://www.mdpi.com/2073-4433/13/3/475>
- [81] I. Prapas, S. Kondylatos, and I. Papoutsis, "Training data for submitted paper "Wildfire Danger Prediction and Understanding with Deep Learning"," May 2022. [Online]. Available: <https://doi.org/10.5281/zenodo.6528394>
- [82] C. Cammalleri, J. V. Vogt, B. Bisselink, and A. de Roo, "Comparing soil moisture anomalies from multiple independent sources over different regions across the globe," *Hydrology and Earth System Sciences*, vol. 21, no. 12, pp. 6329–6343, 2017.
- [83] M. Lin, Q. Chen, and S. Yan, "Network in network," *arXiv preprint arXiv:1312.4400*, 2013.
- [84] Y. Martín, M. Zúñiga-Antón, and M. R. Mimbreno, "Modelling temporal variation of fire-occurrence towards the dynamic prediction of human wildfire ignition danger in northeast spain," *Geomatics, Natural Hazards and Risk*, vol. 10, no. 1, pp. 385–411, 2019. [Online]. Available: <https://doi.org/10.1080/19475705.2018.1526219>
- [85] A. Paszke, S. Gross, F. Massa, A. Lerer, J. Bradbury, G. Chanan, T. Killeen, Z. Lin, N. Gimeshein, L. Antiga, A. Desmaison, A. Kopf, E. Yang, Z. DeVito, M. Raison, A. Tejani, S. Chilamkurthy, B. Steiner, L. Fang, J. Bai, and S. Chintala, "Pytorch: An imperative style, high-performance deep learning library," in *Advances in Neural Information Processing Systems 32*. Curran Associates, Inc., 2019, pp. 8024–8035. [Online]. Available: <http://papers.neurips.cc/paper/9015-pytorch-an-imperative-style-high-performance-deep-learning-library.pdf>
- [86] D. P. Kingma and J. Ba, "Adam: A method for stochastic optimization," *CoRR*, vol. abs/1412.6980, 2015.
- [87] L. Breiman, "Random forests," *Machine Learning* 2001 45:1, vol. 45, pp. 5–32, 10 2001. [Online]. Available: <https://link.springer.com/article/10.1023/A:1010933404324>
- [88] T. Chen and C. Guestrin, "Xgboost: A scalable tree boosting system," in *Proceedings of the 22nd ACM SIGKDD International Conference on Knowledge Discovery and Data Mining*, ser. KDD '16. New York, NY, USA: Association for Computing Machinery, 2016, p. 785–794. [Online]. Available: <https://doi.org/10.1145/2939672.2939785>



Mohamad Hakam Shams Eddin is a PhD student at the University of Bonn, Germany. He received his Dipl.-Ing. degree in topographic engineering from the University of Aleppo, Syria, in 2015 and his M.Sc. degree in geomatics engineering from the University of Stuttgart, Germany, in 2019. His research interests include deep learning, remote sensing, and anomaly detection.



Ribana Roscher (Member, IEEE) received the Dipl.Ing. and Ph.D. degrees in geodesy from the University of Bonn, Bonn, Germany, in 2008 and 2012, respectively. Until 2022, she was a Junior Professor of Remote Sensing with the University of Bonn. Before she was a Postdoctoral Researcher with the University of Bonn, the Julius-Kuehn Institute, Siebeldingen, Germany, Freie Universitaet Berlin, Berlin, Germany, and the Humboldt Innovation, Berlin. In 2015, she was a Visiting Researcher with the Fields Institute, Toronto, ON, Canada.

Since 2022, Ribana Roscher is a professor of Data Science for Crop Systems at the University of Bonn, Bonn, Germany. Currently, she leads the Data Science research area at IBG-2, Forschungszentrum Jülich.



Juergen Gall (Member, IEEE) received his B.Sc. and M.Sc. degrees in mathematics from the University of Wales Swansea, UK and from the University of Mannheim, Germany, in 2004 and 2005, respectively. In 2009, he obtained a Ph.D. in computer science from the Saarland University and the Max Planck Institut fuer Informatik. He was a postdoctoral researcher at the Computer Vision Laboratory, ETH Zurich, Switzerland from 2009 until 2012 and a senior research scientist at the Max Planck Institute for Intelligent Systems in Tuebingen from 2012 until

2013.

Since 2013, Juergen Gall is a professor at the University of Bonn and head of Computer Vision Group.